CrossMark
click for updates

Immune cell screening of a nanoparticle library improves atherosclerosis therapy

Jun Tang[a,b], Samantha Baxter[a], Arjun Menon[c], Amr Alaarg[a,d], Brenda L. Sanchez-Gaytan[a], Francois Fay[a], Yiming Zhao[a], Mireille Ouimet[c], Mounia S. Braza[a], Valerie A. Longo[e], Dalya Abdel-Atti[b], Raphael Duivenvoorden[a], Claudia Calcagno[a], Gert Storm[d,f], Sotirios Tsimikas[g], Kathryn J. Moore[c], Filip K. Swirski[h], Matthias Nahrendorf[h], Edward A. Fisher[c], Carlos Pérez-Medina[a], Zahi A. Fayad[a], Thomas Reiner[b], and Willem J. M. Mulder[a,i,1]

[a]Translational and Molecular Imaging Institute, Icahn School of Medicine at Mount Sinai, 1470 Madison Avenue, New York, NY 10029; [b]Department of Radiology, Memorial Sloan Kettering Cancer Center, 1275 York Avenue, New York, NY 10065; [c]Division of Cardiology, Department of Medicine, Marc and Ruti Bell Program in Vascular Biology, New York University School of Medicine, 550 First Avenue, New York, NY 10016; [d]Department of Biomaterials Science and Technology, MIRA Institute for Biomedical Technology and Technical Medicine, University of Twente, 7500 AE Enschede, The Netherlands; [e]Small-Animal Imaging Core Facility, Memorial Sloan Kettering Cancer Center, 1275 York Avenue, New York, NY 10065; [f]Department of Pharmaceutics, Utrecht Institute of Pharmaceutical Sciences, Utrecht University, 3584 CG Utrecht, The Netherlands; [g]Sulpizio Cardiovascular Center, Department of Medicine, University of California, San Diego, 9434 Medical Center Drive, La Jolla, CA 92037; [h]Center for Systems Biology, Massachusetts General Hospital and Harvard Medical School, Simches Research Building, 185 Cambridge Street, Boston, MA 02114; and [i]Department of Medical Biochemistry, Academic Medical Center, Meibergdreef 9, 1105 AZ Amsterdam, The Netherlands

Edited by Liangfang Zhang, University of California, San Diego, La Jolla, CA, and accepted by Editorial Board Member Mark E. Davis September 12, 2016 (received for review June 14, 2016)

Immunological complexity in atherosclerosis warrants targeted treatment of specific inflammatory cells that aggravate the disease. With the initiation of large phase III trials investigating immunomodulatory drugs for atherosclerosis, cardiovascular disease treatment enters a new era. We here propose a radically different approach: implementing and evaluating in vivo a combinatorial library of nanoparticles with distinct physiochemical properties and differential immune cell specificities. The library's nanoparticles are based on endogenous high-density lipoprotein, which can preferentially deliver therapeutic compounds to pathological macrophages in atherosclerosis. Using the apolipoprotein E-deficient (*Apoe*$^{-/-}$) mouse model of atherosclerosis, we quantitatively evaluated the library's immune cell specificity by combining immunological techniques and in vivo positron emission tomography imaging. Based on this screen, we formulated a liver X receptor agonist (GW3965) and abolished its liver toxicity while still preserving its therapeutic function. Screening the immune cell specificity of nanoparticles can be used to develop tailored therapies for atherosclerosis and other inflammatory diseases.

nanomedicine | drug delivery | immunotherapy | molecular imaging | atherosclerosis

Research in the past decades has revealed the immune system's central role in the pathophysiology of cancer (1), diabetes (2), and atherosclerosis (3, 4). Because macrophages drive pathological progression of these diseases, immunomodulatory small-molecule compounds modulating macrophage function are promising therapeutic candidates for treating these maladies. However, these compounds' lack of cellular specificity necessitates a strategy for targeted delivery to harmful immune cells without negatively affecting beneficial immune cells. Despite numerous studies of nanoparticle-based delivery, rational attempts to screen meticulously designed nanoparticles for immune cell specificity in vivo have never been reported.

We created a combinatorial library of hybrid lipoprotein-inspired nanoparticles with distinct physiochemical properties (particularly size and chemical composition) with differential immune cell specificity. We then chose atherosclerosis, a lipid-driven inflammatory process of the large arteries, as a model disease to evaluate our nanoparticle library. Atherosclerosis accounts for the majority of cardiovascular deaths worldwide (5), and macrophages are the major immune cells to drive the pathological inflammation and the progression of atherosclerotic plaques (6, 7). These plaques, which are present throughout the vasculature, have a complicated cellular composition (8). To improve the therapeutic index of small-molecule immunomodulatory compounds, plaque macrophage-specific delivery, with minimal delivery to nonpathological cells in healthy tissues, is essential.

We used the apolipoprotein E-deficient (*Apoe*$^{-/-}$) mouse model of atherosclerosis to evaluate our nanoparticle library, because it accurately recapitulates some important immunological aspects of human atherosclerosis (9). Using a combination of optical methods, immunological techniques, and in vivo positron emission tomography (PET) imaging, we carefully selected candidate nanoparticles from the library for subsequent atherosclerosis drug delivery studies. As a proof of concept, we incorporated the liver X receptor agonist GW3965, a therapeutic compound that did not reach clinical application due to its serious adverse effects on the liver (10, 11), in two nanoparticles—one with favorable organ distribution and immune cell specificity and one without. In *Apoe*$^{-/-}$ mice with advanced disease, the favorable nanoparticle from the library screen was

Significance

The immune system plays an essential role in the pathophysiology of major diseases such as atherosclerosis, diabetes, and cancer, which has inspired the development of numerous small molecules to modulate immune cells, intending to create immunotherapies for these diseases. Tissue- and cell-specific delivery of these small molecules is the key to transform these compounds to safe, potent immunotherapies. In this study, we present an in vivo nanoparticle screen approach that involves designing and evaluating a library of nanoparticles with distinct immune cell targeting specificity. This study carries out a systematic in vivo immune cell screening to create effective nanoparticle-based immunotherapy for modulating the pathological immune cells in atherosclerosis.

Author contributions: J.T., G.S., S.T., K.J.M., F.K.S., M.N., E.A.F., C.P.-M., Z.A.F., T.R., and W.J.M.M. designed research; J.T., S.B., A.M., A.A., B.L.S.-G., F.F., Y.Z., M.O., M.S.B., V.A.L., D.A.-A., and C.P.-M. performed research; J.T., C.C., S.T., K.J.M., E.A.F., Z.A.F., T.R., and W.J.M.M. contributed new reagents/analytic tools; J.T., A.M., B.L.S.-G., M.O., R.D., F.K.S., M.N., E.A.F., C.P.-M., T.R., and W.J.M.M. analyzed data; J.T., S.B., C.P.-M., and W.J.M.M. wrote the paper; and W.J.M.M. supervised the whole project.

The authors declare no conflict of interest.

This article is a PNAS Direct Submission. L.Z. is a Guest Editor invited by the Editorial Board.

[1]To whom correspondence should be addressed. Email: Willem.mulder@mssm.edu.

This article contains supporting information online at www.pnas.org/lookup/suppl/doi:10.1073/pnas.1609629113/-/DCSupplemental.

ENGINEERING
IMMUNOLOGY AND INFLAMMATION
Downloaded at Palestinian Territory, occupied on November 25, 2021
www.manaraa.com

shown to abolish GW3965's liver toxicity while remaining effective on atherosclerotic plaque macrophages.

Results

Study Design. We created a combinatorial library comprising 15 high-density lipoprotein-mimicking nanoparticles and two extensively studied nanoparticles, a PEGylated micellar and a long-circulating liposomal nanoparticle. We then combined in vitro assays and in vivo experiments in atherosclerotic *Apoe*$^{-/-}$ mice to study the nanoparticle library's biological behavior by using near-infrared fluorescence imaging (NIRF), flow cytometry, immunofluorescence, and radiolabeling. Based on the results of this library screening, we formulated two GW3965-loaded HDL nanoparticles with distinctly different immune cell specificity and organ distribution. Finally, we quantitatively studied the pharmacokinetics, immune cell specificity, liver toxicity, and therapeutic effects of these drug-loaded nanoparticles in *Apoe*$^{-/-}$ mice with advanced atherosclerosis (Fig. 1*A*).

HDL Nanoparticle Library. Previous studies indicate that the size, phospholipid composition, ratio of phospholipid to apolipoprotein A-1 (APOA1), or the inclusion of payloads can affect HDL-mimicking nanoparticles' in vivo performance (12–14). In our current study, we created a library containing HDL-mimicking nanoparticles that differ in size, shape, composition, and payload, all of which have been reported to affect nanoparticles'

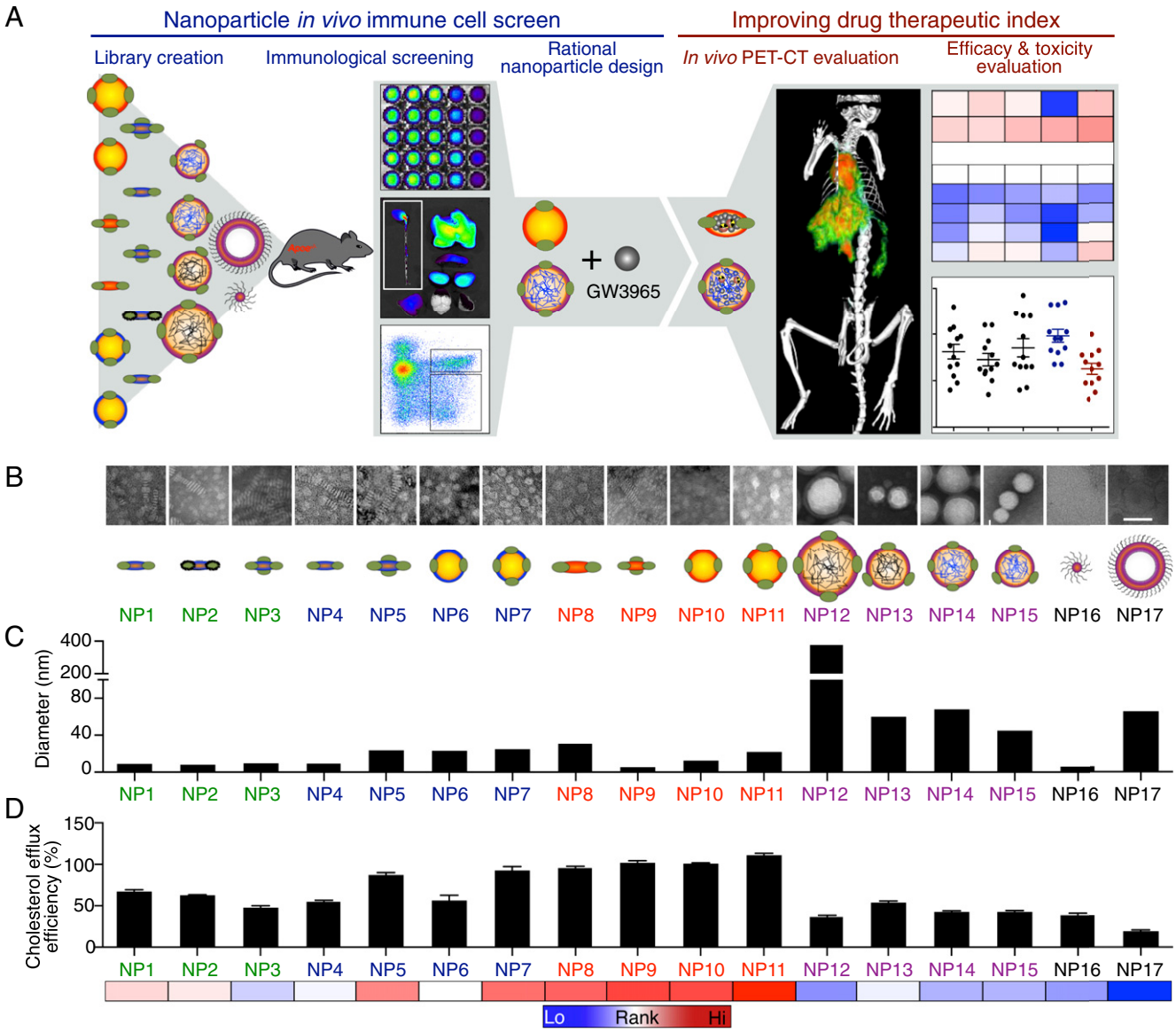

Fig. 1. Study design and in vitro characterization of the nanoparticle library. (*A*) In the in vivo immune cell screen study (left), we first created a combinatorial nanoparticle library and then evaluated the library in atherosclerotic *Apoe*$^{-/-}$ mice by using blood half-life determination, NIRF, and flow cytometry. The library screening data lead to rational design of one GW3965-loaded nanoparticle with favorable characteristics and one without. In the second study, the two nanoparticles were radio- and fluorescence-labeled, and they were quantitatively and therapeutically evaluated by using PET-CT imaging, mRNA profiling, flow cytometry, and liver toxicity assays (right). (*B*) Representative high-magnification TEM images of negatively stained nanoparticles. Low-magnification images and a discussion of the different structures are presented in Fig. S1. (Scale bar, 50 nm.) (*C*) The size of nanoparticles as measured by dynamic laser scattering (DLS). (*D*) Cholesterol efflux capacity of the nanoparticles in primary macrophages normalized to natural human HDL ($n = 6$). Error bars are SDs. Color-coded bar at the bottom shows the relative rank of each nanoparticle, with the red indicating high cholesterol efflux efficiency and the blue indicating low efficiency.

Downloaded at Palestinian Territory, occupied on November 25, 2021
www.manaraa.com

in vivo targeting efficiency (15). To fine-tune nanoparticle size and morphology, we added either triglyceride or polymers [polylactic-*co*-glycolic acid (PLGA) or polylactic acid (PLA)] to the HDL core (Table S1); this allowed us to modulate nanoparticle size from about 10 nm (NP1, NP2, NP3, and NP9) or 30 nm (NP6, NP7, NP10, and NP11) to over 100 nm (NP12) (Fig. 1 *B* and *C*). We observed that the inclusion of a core component, namely triglycerides or polymers, results in a nanoparticle shape change from discoidal to spherical, as can be clearly appreciated when comparing NP5 to NP7 and NP15. In addition to size and shape, we also varied phospholipid composition (Table S1). Because oxidization greatly affects HDL function (16), we

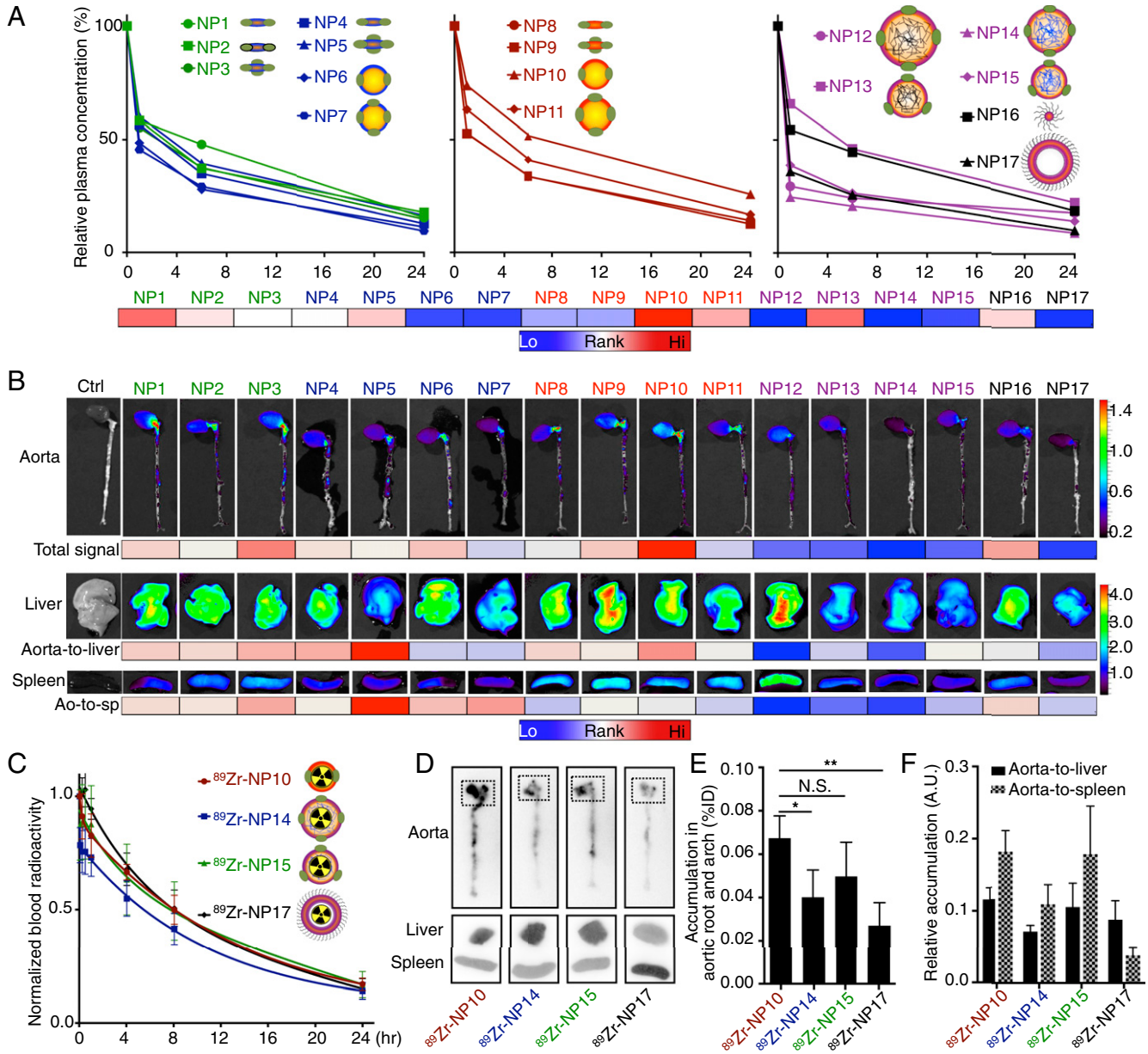

Fig. 2. In vivo evaluation of the nanoparticle library. (*A*) Relative nanoparticle plasma concentration in *Apoe*$^{-/-}$ mice that were fed a 12-wk high-cholesterol diet. The values were derived from the near-infrared dye DiR incorporated in the nanoparticles. Heat map below the graphs ranks the blood half-lives, with the red indicating a long and the blue a short blood half-life ($n = 5$ per nanoparticle). The values of blood half-lives are provided in Table S2. (*B*) Representative near-infrared fluorescence images of nanoparticle accumulation in aorta, liver, and spleen. The heat map below the aorta images ranks the mean total fluorescent tissue signal, the heat map below the liver images ranks the total aorta-to-liver signal, and the heat map below the spleen images ranks the mean aorta-to-spleen accumulation (Ao-to-sp) ratio, with the red indicating a high and the blue a low ratio ($n = 5$ for each nanoparticle). Bar graphs are provided in Fig. S2. (*C*) Blood half-lives of four selected nanoparticles radiolabeled with ^{89}Zr ($n = 3$ per nanoparticle) were 7.0 h for ^{89}Zr-NP10, 5.7 h for ^{89}Zr-NP14, 7.1 h for ^{89}Zr-NP15, and 6.6 h for ^{89}Zr-NP17. Blood radioactivity (percentage injected dose per gram of tissue) of all time points is normalized to that of the first time point—2 min after injection. (*D*) Representative autoradiography images of aortas, livers, and spleens 24 h after nanoparticle injection. Dashed windows indicate the aortic root and arch area analyzed in *E*. (*E*) Nanoparticle accumulation in aortic roots and arches as measured by percentage of injected dose (%ID) ($n = 3$ per nanoparticle). (*F*) Relative accumulation of nanoparticles between aortas and liver or spleen. Arbitrary units (A.U.) were defined by the aortic accumulation (percentage injected dose per gram of tissue) divided by the hepatic or splenic accumulation (percentage injected dose per gram of tissue). Error bars are SDs. Statistics was calculated with nonparametric two-tailed Student's *t* test. N.S., not statistically significant; $*P < 0.05$; $**P < 0.01$.

Downloaded at Palestinian Territory, occupied on November 25, 2021
www.manaraa.com

sought to test if this modification also changed the HDL-mimicking nanoparticles' drug delivery capability. We oxidized the phospholipids and APOA1 of NP1 to produce NP2 (Fig. S1*B*). The nanoparticle sizes were measured by dynamic light scattering, and their morphologies were visualized by transmission electron microscopy (TEM) (Fig. 1 *B* and *C*). Micellar (17) and liposomal (18) nanoparticles are established lipid-based platforms and served as references in this study.

HDL Nanoparticle Library's Cholesterol Efflux Efficiency. Natural HDL facilitates reverse cholesterol transport, the intrinsic mechanism that removes cholesterol from macrophages in atherosclerotic plaques and protects against the atherosclerosis (19, 20). Cholesterol efflux capacity indicates the nanoparticles' biological similarity to native HDL. Therefore, we measured the 17 nanoparticles' ability to induce cholesterol efflux from cholesterol-laden primary macrophages. We found 1-palmitoyl-2-oleoyl-*sn*-glycero-3-phosphocholine (POPC)-based nanoparticles (NP8, NP9, NP10, and NP11) to be the most efficient in extracting cholesterol from macrophages; in contrast, polymer-core HDL nanoparticles produced the least cholesterol efflux (NP12, NP13, NP14, and NP15). Liposomal and micellar nanoparticles, without APOA1 on their surface to bind the cholesterol efflux receptors Abca1 and Abcg1, performed similarly to polymer-core HDL nanoparticles (Fig. 1*D*). These results demonstrate the essential role of APOA1, as well as the impact of phospholipid and core composition, in promoting cholesterol efflux. It has been proposed that APOA1 changes conformation when interacting with its specific receptors to extract cholesterol (19). The artificial polymeric cores of NP12, NP13, NP14, and NP15 might limit conformational flexibility of APOA1, leading to impaired cholesterol efflux. On the other hand, POPC-based HDL nanoparticles display less rigidity, are more similar to natural HDL, and therefore result in more efficient cholesterol efflux.

Nanoparticles' Physiochemical Properties Affect Their in Vivo Behavior. We i.v. injected the library's 1,1′-dioctadecyl-3,3,3′,3′-tetramethylindotricarbocyanine iodide (DiR)-labeled nanoparticles into atherosclerotic *Apoe*$^{-/-}$ mice. We found that NP1 and NP10, with diameters between 7 nm and 30 nm, exhibited the longest blood half-lives of 5.0 h and 6.3 h, respectively. NP12 and NP14, with diameters larger than 70 nm, had the shortest blood half-lives of 0.71 h and 0.67 h, respectively (Fig. 2*A*). The difference between the longest and the shortest blood half-life was almost 10-fold (Table S2).

Using NIRF, we investigated nanoparticle accumulation in the heart, aorta, lung, liver, spleen, kidney, brain, and muscle 24 h after i.v. administration (Fig. 2*B* and Fig. S2*A*). Among all nanoparticles, liver accumulation was generally the highest, followed by spleen, kidney, and lung accumulation (Fig. S2*B*). Because the aorta is the primary target tissue whereas the liver and spleen are clearance organs, we determined accumulation in the aorta relative to these two organs (21). Our measurements showed a 3.4-fold difference between the highest and lowest aorta-to-liver accumulation ratios (NP5 vs. NP12, $P < 0.01$, Fig. S2*D*), and a 4.7-fold difference between the aorta-to-spleen accumulation ratios (NP5 vs. NP12, $P < 0.01$, Fig. S2*E*). For the nanoparticles' relative performance, see Fig. 2*B*. Distribution of DiR-labeled nanoparticle in certain tissues is difficult to quantify in vivo due to the limited penetrating depth of light and varying absorbance rates among tissues (22). Radiolabeled nanoparticles' biodistribution and pharmacokinetics can be quantitatively measured. From our initial optical imaging screen, we selected NP10, NP14, NP15, and NP17 to be labeled with Zr through the hydrophobic chelator deferoxamine (DFO)-C34, which serves as a surrogate for hydrophobic payloads. In line with the optical imaging results, we observed that the smaller nanoparticles (NP10 and NP15) had longer blood half-lives than the larger ones (NP14 and NP17, Fig. 2*C*). We also observed that the HDL-based nanoparticles (NP10, NP14, and NP15), particularly NP10, accumulated more efficiently in atherosclerotic plaques than the liposomal nanoparticle (Fig. 2 *D* and *E*). Overall, NP10 displayed the most favorable performance among the four selected nanoparticles (Fig. 2 *C*–*F*).

Distinct Immune Cell Targeting Patterns Within the Nanoparticle Library. Macrophages and monocytes are the key immune cells that drive atherosclerosis progression (4). In *Apoe*$^{-/-}$ atherosclerotic mice, these cells mainly reside in atherosclerotic plaques, spleen, blood, and bone marrow (4). Using a robust flow cytometry procedure adapted from previous studies (23, 24), we were able to identify macrophages, monocytes, and nonmyeloid immune cells (Lin^{+}) in the aortas; macrophages, Ly-6C^{hi} monocytes, dendritic cells (DCs), and neutrophils in the spleens; and Ly-6C^{hi} monocytes, Ly-6C^{lo} monocytes, DCs, and neutrophils in the blood (Fig. 3*A*).

In the aortas, all HDL-mimicking nanoparticles efficiently targeted macrophages and monocytes. The difference between the highest and lowest nanoparticle accumulations was 5.7-fold in macrophages (NP3 vs. NP17, $P < 0.01$) and 2.7-fold in monocytes (NP3 vs. NP7, $P < 0.001$; Fig. 3*B*). In the spleens, all nanoparticles had the highest accumulation in macrophages, which do the bulk of nanoparticle clearance, with a 3.8-fold difference between the highest and lowest accumulation levels (NP12 vs. NP17, $P < 0.01$, Fig. 3*B*). In the blood, DCs and Ly-6C^{hi} monocytes displayed the highest nanoparticle association, with a 3.8-fold difference between the highest and lowest association levels (NP10 vs. NP5, $P < 0.01$) in DCs and a 3.79-fold difference in Ly-6C^{hi} monocytes (NP3 vs. NP14, $P < 0.0001$, Fig. 3*B*). In addition, the nanoparticles were far less effective in targeting Ly-6C^{lo} monocytes, the patrolling monocytes in the blood, compared with Ly-6C^{hi} monocytes (Fig. 3*B*).

Although aortic macrophages are the main target of immunomodulatory nanoparticles, splenic macrophages, which clear nanoparticles from the blood and reduce their bioavailability to aortic macrophages (25), need to be avoided. We evaluated the ratios of nanoparticle accumulation in aortic macrophages versus splenic macrophages, and we found a 3.8-fold difference between the highest and lowest aortic-to-splenic ratios (NP16 vs. NP12, $P < 0.0001$, Fig. S3*A*). This differential targeting specificity to atherosclerotic macrophages was confirmed by immunofluorescence in the aortic roots (Fig. S3*B*). Altogether, the flow cytometry data reveal that the distinct physiochemical nanoparticle properties within the library lead to drastically different immune cell targeting patterns (Fig. 3*C*).

GW3965-Loaded Nanoparticle Development. Liver X receptor (LXR) agonists promote cholesterol efflux from macrophages in atherosclerotic plaques, and they have been proposed as novel immunomodulatory drugs for the disease (26). However, most experimental LXR agonists fail clinical translation or early-stage clinical trials due to poor safety profiles. For example, GW3965, an effective LXR agonist promoting cholesterol efflux from atherosclerotic macrophages (27, 28), did not reach the clinical phase, because of its liver toxicity in hamsters and monkeys (10), as well as in human hepatocytes (11).

In our nanoparticle library studies, NP10 was found to have high cholesterol efflux promotion efficiency, a long blood half-life, high relative aorta-to-liver accumulation, and a high relative aortic-to-splenic macrophage association ratio (Fig. S4*A*). These features make NP10 a promising candidate for avoiding GW3965's liver toxicity and enhancing its efficacy on atherosclerotic plaque macrophages. Therefore, we replaced NP10's hydrophobic triglyceride cargo with hydrophobic GW3965 and created a GW3965-loaded nanoparticle (Rx-HDL) that was morphologically similar but not identical, due to the different nanoparticle composition, to NP10 in size (~30 nm), phospholipid composition (POPC-dominant), and morphology (Fig. S4*B*). Further, we identified NP14 as an unfavorable nanoparticle for GW3965 delivery due to the nanoparticle's poor cholesterol efflux efficiency, short blood half-life,

Downloaded at Palestinian Territory, occupied on November 25, 2021
www.manaraa.com

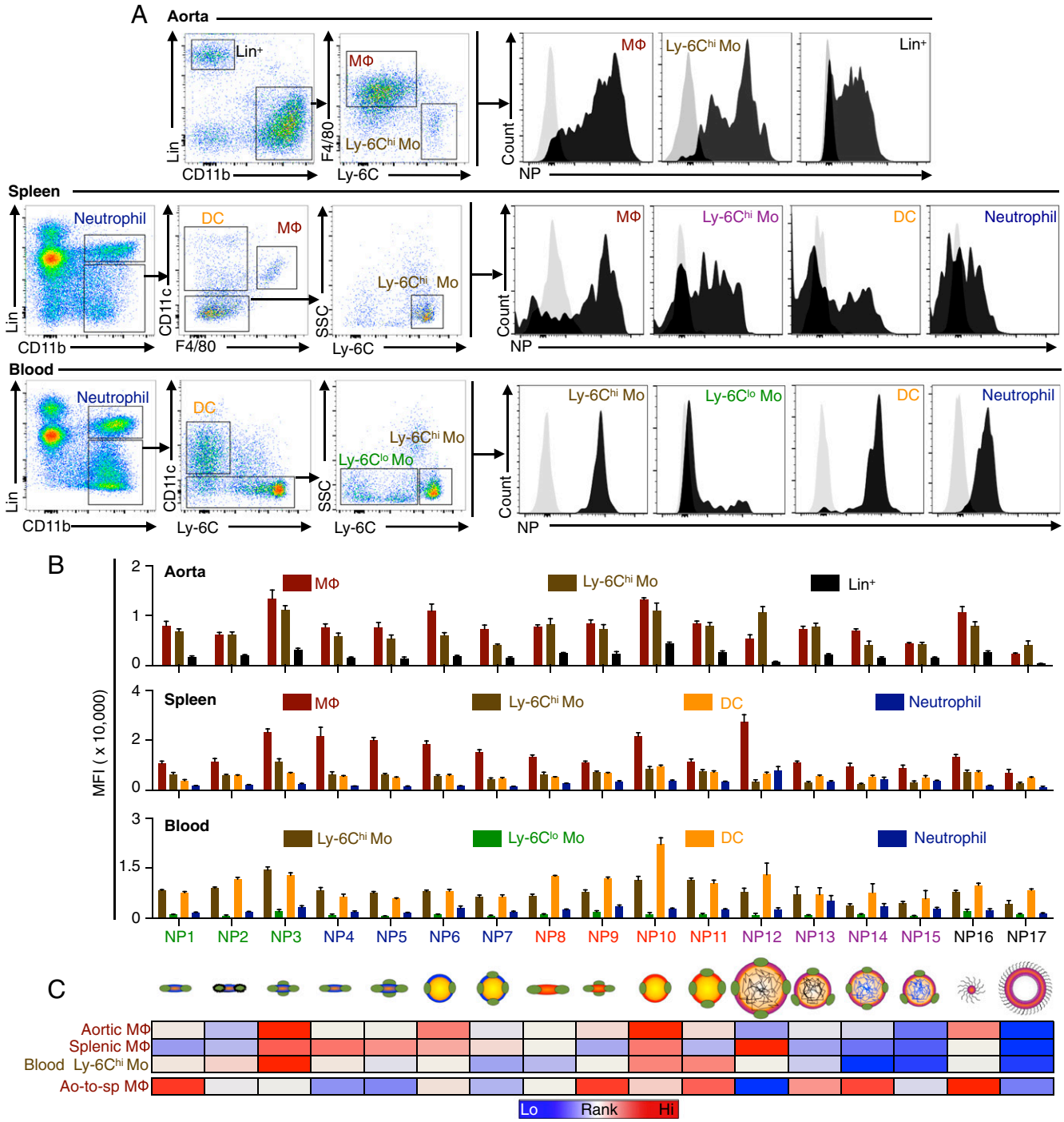

Fig. 3. Nanoparticle immune cell specificity. (*A*) The flow cytometry gating procedures to identify relevant immune cells in aorta, spleen, and blood. Black histograms on the right show representative signal distribution of different immune cells in the mice injected with nanoparticles compared with the cells from control animals injected with PBS (gray histogram on the left in each graph). (*B*) Quantification of mean fluorescence intensity (MFI) of each immune cell type in different tissues; $n = 5$ for each nanoparticle, and error bars are SEMs. (*C*) Heat map ranks targeting efficiency in key immune cells (aortic macrophages, spleen macrophages, and blood Ly-6C^{hi} monocytes), with red indicating a high and blue indicating a low MFI in the first three rows. The last row shows the aortic-to-splenic macrophage MFI ratio (Ao-to-sp MΦ), and its quantitative values are provided in Fig. S3*A*.

and low relative aorta-to-liver accumulation (Fig. S4*A*). By loading GW3965 into the PLGA matrix of NP14, we created a PLGA-core GW3965-loaded nanoparticle (Rx-PLGA-HDL) with similar size, phospholipid composition, and morphology to NP14 (Fig. S4*B*). Notably, the size and cholesterol efflux capability of the two drug-loaded nanoparticles were drastically different (Fig. S4 *B* and *C*).

Quantitative Evaluation of GW3965-Loaded Nanoparticles. Nanoparticles that are ^{89}Zr-labeled can be quantitatively characterized by in vivo PET imaging as well as by ex vivo radioactivity counting (29). To accurately understand the in vivo performance of the two nanoparticles, we loaded the hydrophobic ^{89}Zr-DFO-C34 into Rx-HDL and Rx-PLGA-HDL (Fig. 4*A*), and radioactive high-performance chromatography showed

Downloaded at Palestinian Territory, occupied on November 25, 2021

المنارة للاستشارات
www.manaraa.com

both Rx-HDL and Rx-PLGA-HDL to be efficiently radiolabeled (Fig. S4*D*).

In *Apoe*$^{-/-}$ atherosclerotic mice, Rx-HDL circulated in the blood much longer (weighted $t_{1/2}$ = 10.5 h, n = 3) than Rx-PLGA-HDL (weighted $t_{1/2}$ = 5.0 h, n = 3, Fig. 4*B*) or its precursor NP10 ($t_{1/2}$ = 7.0 h, Fig. 2*C*), demonstrating its favorable features. We then used PET-computed tomography hybrid imaging (PET-CT) to measure the nanoparticle dynamic accumulation in the cardiac blood pool, the liver, and the spleen 30 min and 24 h after i.v. administration (n = 5 per nanoparticle, Fig. 4*C*; also see Movies S1–S4). After 30 min, Rx-HDL had higher accumulation in the cardiac blood pool (29.9 maximum percentage injected dose per gram of tissue (Max %ID/g) vs. 24.5 Max %ID/g, $P < 0.05$) but lower accumulation in the liver than Rx-PLGA-HDL (21.7 Max %ID/g vs. 29.7 Max %ID/g, $P < 0.05$). After 24 h, Rx-HDL liver accumulation was still 36% lower than Rx-PLGA-HDL (26.5 Max %ID/g vs. 41.7 Max %ID/g, $P < 0.05$, Fig. 4 *C* and *D*). Autoradiography revealed that both nanoparticles displayed patchy aorta accumulation, in accordance with the heterogeneous distribution of atherosclerotic plaques in this tissue (30) (Fig. 4*E*). Additionally, autoradiography confirmed the highest nanoparticle accumulation to be in the liver and spleen (Fig. 4*E*), a result that was corroborated by an extensive biodistribution analysis (Fig. S4*E*).

Having labeled both nanoparticles with DiR (Fig. 4*A*), we used our flow cytometry protocol (Fig. 3*A*) to quantify immune cell targeting specificity (Fig. S4*F*). Rx-HDL predominantly targeted macrophages in the aortas, and its accumulation was twofold higher than Rx-PLGA-HDL ($P < 0.01$). In the spleen, Rx-HDL had 33% less accumulation in splenic macrophages than Rx-PLGA-HDL ($P < 0.05$). In the blood, Rx-HDL targeted Ly-6C^{hi} monocytes 2.4-fold more efficiently than Rx-PLGA-HDL ($P < 0.01$, Fig. 4 *F* and *G*). Collectively, these data show that, compared with Rx-PLGA-HDL, Rx-HDL has a longer blood half-life, lower accumulation in the liver, higher accumulation in atherosclerotic plaque macrophages, and lower accumulation in splenic macrophages.

Nanoparticle Abolishes Liver Toxicity and Preserves Efficacy of GW3965. To test if Rx-HDL's optimal in vivo performance reduced GW3965s liver toxicity, we gave four i.v. injections (one injection every 2 d, at a dose of 10 mg/kg GW3865) of Rx-HDL, its

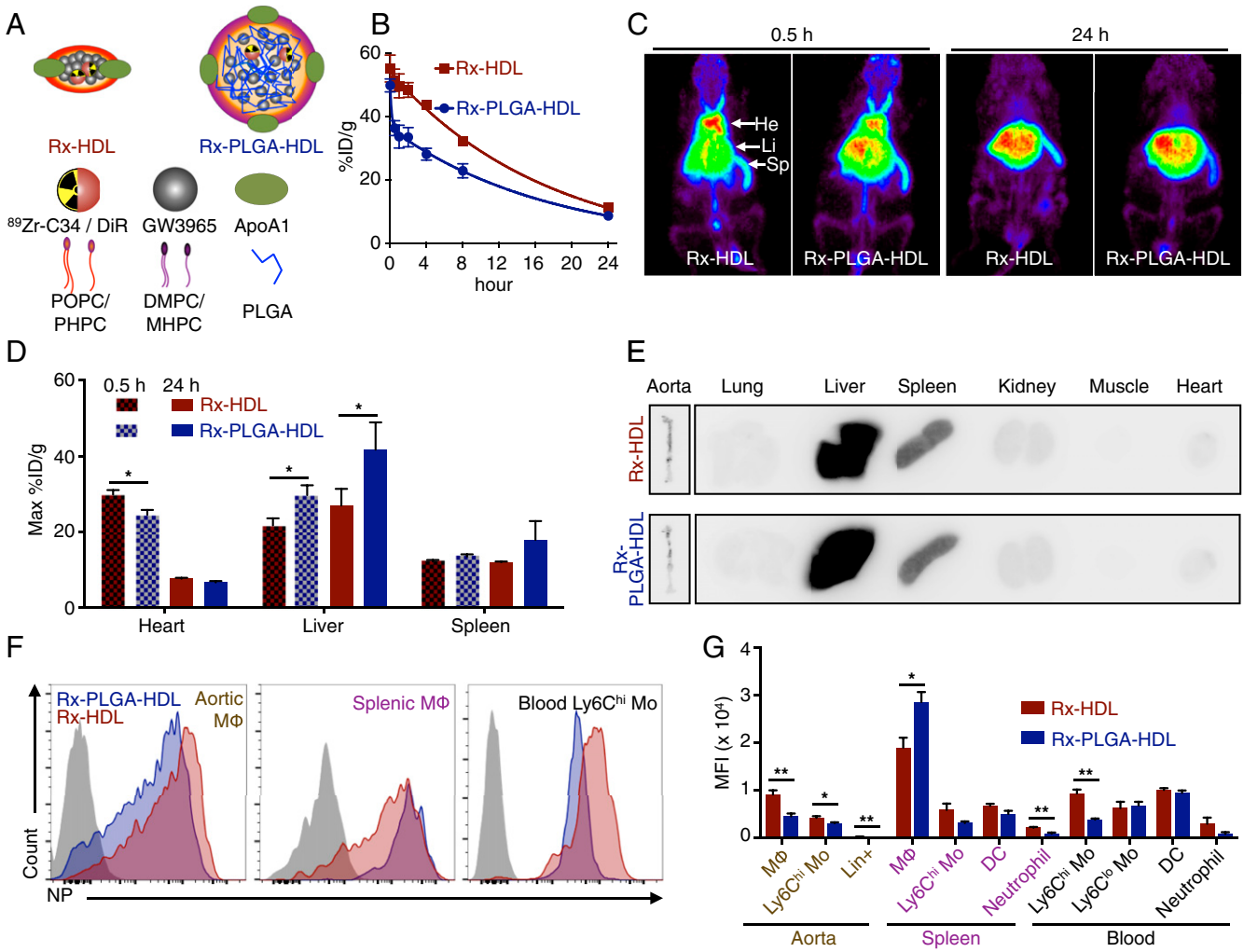

Fig. 4. In vivo quantitative evaluation of GW3965-loaded nanoparticles. (*A*) Schematic depictions of small Rx-HDL plaque macrophage-targeting and large polymer-hybrid Rx-PLGA-HDL nanoparticles. The two nanoparticles were either radiolabeled with ^{89}Zr or labeled with the near-infrared fluorescent dye DiR. (*B*) Blood half-lives were determined in three mice per nanoparticle. (*C*) Representative PET images of mice that received either the small or large nanoparticle at 0.5 h and 24 h after i.v. administration. The 3D-rendered images are provided as Movies S1–S4 (n = 5 per nanoparticle). (*D*) Quantification of radioactivity in the heart, liver, and spleen. (*E*) Representative autoradiographic images of key organs. Full biodistribution of all organs is provided in Fig. S4*E*. (*F*) Representative histograms of selected immune cell targeting specificity in the aorta, spleen, and blood. (*G*) MFI quantification of relevant immune cells in the tissues (n = 4 per nanoparticle). Error bars are SEM. Statistics was calculated with nonparametric two-tailed Student's t test. *$P < 0.05$; **$P < 0.01$.

Downloaded at Palestinian Territory, occupied on November 25, 2021
www.manaraa.com

vehicle control (HDL), Rx-PLGA-HDL, its vehicle control (PLGA-HDL), and PBS to *Apoe*$^{-/-}$ atherosclerotic mice (n = 12 per group).

In the liver, Rx-PLGA-HDL increased the expression of two of the three major GW3965-related toxicity genes, and Rx-HDL increased the expression of one gene (Fig. 5*A*). Importantly, we measured hepatic triglyceride and cholesterol levels, which are the major biomarkers of GW3965-induced hepatic steatosis (10). The Rx-PLGA-HDL group had 35.4% more hepatic triglyceride than its control vehicle PLGA-HDL group (P = 0.014) and 21% more than the PBS group (P = 0.12). For hepatic cholesterol, the Rx-PLGA-HDL group had 31% higher levels than the PLGA-HDL group (P = 0.018) and 17% higher levels than the PBS group (P = 0.014). These results suggest that the high liver accumulation of Rx-PLGA-HDL caused severe liver toxicity (Fig. 5 *B* and *C*). On the other hand, the Rx-HDL group had 26.5% lower hepatic triglyceride levels than its vehicle HDL control group (P = 0.06) and 22.7% lower levels than the PBS group (P = 0.076). The Rx-HDL group also had 20% lower hepatic cholesterol levels than the HDL group (P = 0.06) and 33.3% lower levels than the PBS group (P = 0.00043). A recent study suggested that high HDL levels are associated with a lower degree of steatosis, which might explain the reduced hepatic triglyceride and cholesterol levels in mice treated with vehicle HDL nanoparticles (31). Furthermore, GW3965 has been reported to increase HDL levels in mice (32), likely explaining the additional hepatic benefits in Rx-HDL-treated mice. Most importantly, compared with the Rx-PLGA-HDL group, the Rx-HDL group had 36.1% lower hepatic triglyceride (P = 0.00083) and 43.0% lower hepatic cholesterol levels (P < 0.0001). These results demonstrate that the two GW3965-loaded nanoparticles' distinct liver accumulations resulted in differential liver toxicity profiles (Fig. 5 *A*–*C*).

To measure the treatments' efficacies on aortic macrophages, we isolated the cells from aortic roots by laser capture microdissection and measured their mRNA expression levels by quantitative real-time PCR (qPCR). We found that Rx-HDL increased expression

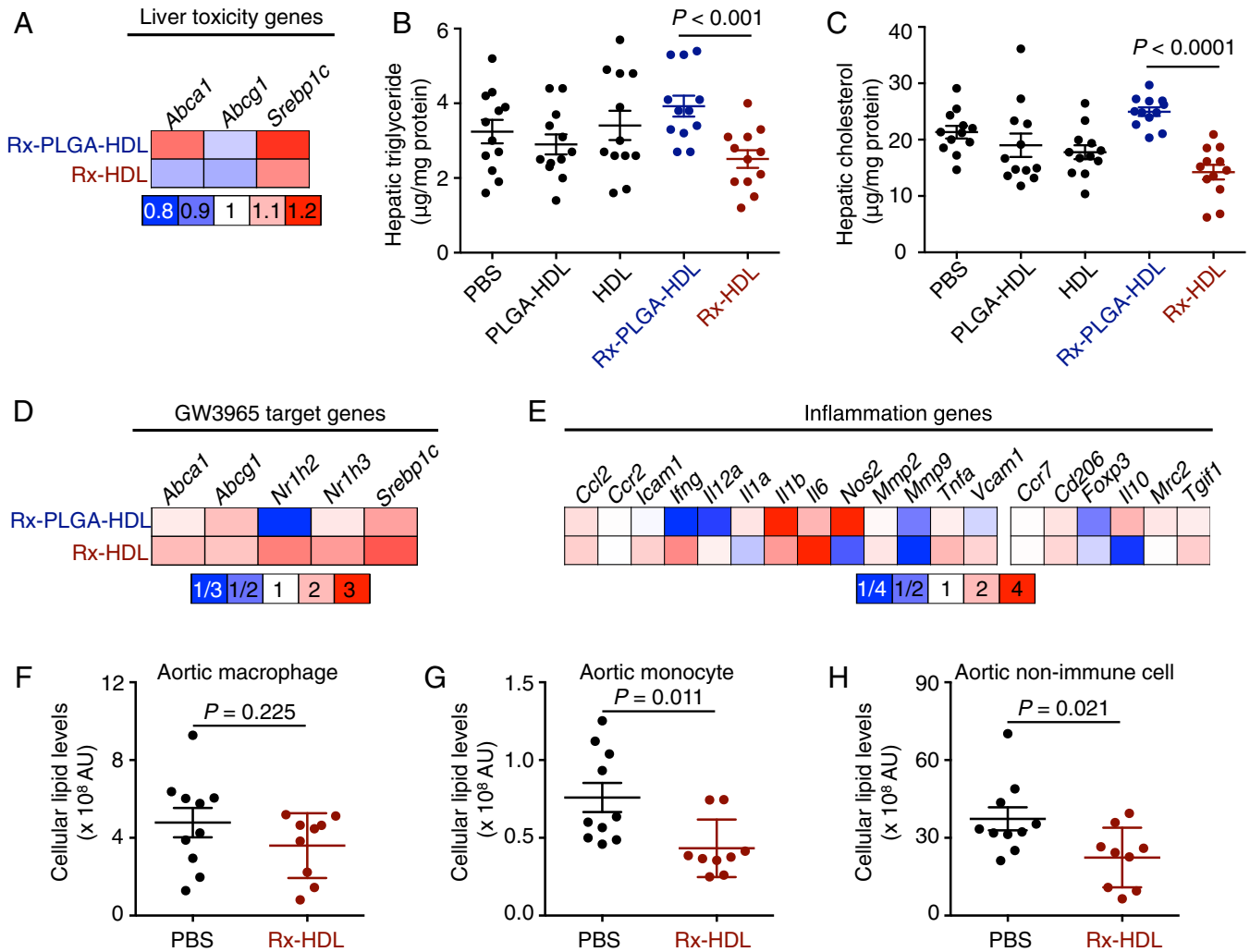

Fig. 5. Evaluation of the toxicity and efficacy of GW3965 (Rx)-loaded nanoparticles. In *A*–*E*, *Apoe*$^{-/-}$ mice received four i.v. administrations of nanoparticles or PBS on every other day (n = 12 per group). (*A*) The mRNA expression levels of three GW3965 target genes in liver homogenates. (*B*) Triglyceride and (*C*) cholesterol levels in the liver, the primary organ suffering from the toxic effects of GW3965. (*D*) The mRNA expression levels of five GW3965 target genes in aortic macrophages. (*E*) The mRNA expression levels of 19 inflammation-related genes in aortic macrophages. All gene expression was normalized to housekeeping gene *Hprt1*. The bar graph presentation of the heat maps is in Fig. S5 (n = 12 per group). In *F*–*H*, *Apoe*$^{-/-}$ mice (n = 10 in PBS; n = 9 in Rx-HDL) received 12 i.v. injections in 6 wk. Lipid levels of aortic cells were analyzed by flow cytometry. Cellular lipid levels were calculated by multiplying the mean fluorescence intensity of a cell type by the number of the cells per aorta (AU = MFI × number of cells). The total lipid levels of aortic (*F*) macrophages, (*G*) monocytes, or (*H*) nonimmune CD45^{-} cells per aorta in the mice are presented here. Gating procedure is provided in Fig. S6 *A* and *B*. Error bars in all graphs are SEM. Statistics was calculated with nonparametric two-tailed Student's t test.

Downloaded at Palestinian Territory, occupied on November 25, 2021
www.manaraa.com

of five GW3965 target genes compared with the vehicle HDL control, whereas Rx-PLGA-HDL increased only four genes compared with the vehicle PLGA-HDL control (Fig. 5*D*). Furthermore, Rx-HDL produced elevated expression of the five target genes compared with Rx-PLGA-HDL (Fig. S5 *A* and *B*). These results suggest successful GW3965 delivery to macrophages in atherosclerotic plaques. We did not observe clear effects of either nanoparticle on genes related to macrophage inflammation, as the number of genes with increased expression was almost equal to the number with decreased expression (Fig. 5*E* and Fig. S5 *A* and *B*). Similarly, the macrophage levels in aortic roots were the same among all groups (Fig. S5 *D* and *E*).

Based on the favorable properties of Rx-HDL, we further evaluated its therapeutic effects in a 6-wk, long-term treatment regimen focusing on cellular lipid levels in aortas. Working from a BODIPY (4,4-difluoro-1,3,5,7,8-pentamethyl-4-bora-3a,4a-diaza-*s*-indacene)-based flow cytometry protocol (33), we developed a procedure to quantify the cellular lipid levels of macrophages, monocytes, and CD45 negative nonimmune cells ($CD45^-$) in the aortas (Fig. S6). Importantly, we found that the 6-wk treatment of Rx-HDL (10 mg/kg GW3965, two i.v. injections per week) resulted in 28% less total lipid in aortic macrophages ($P = 0.224$; Fig. 5*F*). Further, the treatment reduced total lipid levels in monocytes by 43.0% ($P = 0.011$, Fig. 5*G*) and in all $CD45^-$ nonimmune cells by 40.0% ($P = 0.021$, Fig. 5*H*). Furthermore, no therapeutic effects were observed when the compound was given orally with the same 6-wk treatment regimen (10 mg/kg GW3965, two gavages per week) compared with the placebo-treated group (Fig. S6 *C–H*). Consistent with the liver toxicity results after the short-term Rx-HDL treatment, blood cholesterol and triglyceride levels were similar to those in mice receiving PBS treatment (Fig. S7 *A* and *B*). In addition, the long-term treatment of Rx-HDL did not cause any observable toxicity in the liver, kidney, heart, and blood cells (Fig. S7 *C–L*). Taken together, the results show that long-term Rx-HDL treatment produces significant therapeutic benefits without causing toxicity in major organs, most notably the liver, whereas long-term oral treatment at the same dose did not produce any therapeutic benefits.

In summary, we developed a rational library screen strategy to identify nanoparticles with favorable immune cell specificity and biodistribution in an atherosclerosis mouse model. On the basis of this nanoparticle screen, we optimized GW3965 delivery to plaque macrophages and, while preserving its efficacy on atherosclerotic plaques (Fig. 5 *D–H*), abolished GW3965 liver toxicity (Fig. 5 *A–C* and Fig. S7), a well-known adverse effect of LXR agonists.

Discussion

By fine-tuning the components and synthesis procedures, we created a combinatorial library of 17 nanoparticles with distinct composition, size, and morphology. These distinct physiochemical properties resulted in an approximate sixfold difference in promoting cholesterol efflux from macrophages, 10-fold difference among blood half-lives, 3.4-fold difference in relative aorta-to-liver accumulation, and 3.8-fold difference in relative aortic-to-splenic macrophage accumulation. From this library screening, we identified the favorable lipid composition (POPC-dominant), pharmacokinetics (long blood half-life), size (around 30 nm), and morphology (spherical) to achieve optimal plaque macrophage-specific drug delivery. We hypothesize that the combination of long blood half-life and small size allow efficient and prolonged atherosclerotic plaque penetration and subsequent macrophage accumulation. A favorable nanoparticle lipid composition and morphology increases stability and promotes delivery of the encapsulated small molecules to the targeted cells, as suggested by our recent study (34). In a proof-of-concept application, we used these guidelines to identify two nanoparticles from the library as the most and least favorable nanoparticles for delivering the liver-toxic compound GW3965. Although the unfavorable nanoparticle Rx-PLGA-HDL caused severe GW3965-induced liver toxicity, the favorable nanoparticle Rx-HDL did not cause observable liver toxicity in treated animals but did preserve the compound's therapeutic efficacy on the atherosclerotic plaques.

Despite the clinical introduction of antibody immunotherapies for atherosclerosis (35), such biological drugs can only modulate a limited number of extracellular targets, such as PCSK9 (36, 37) or receptors on cell surface (38). Intracellular entities present many more immunological targets that can be effectively controlled by immunomodulatory small molecules. Most experimental small molecules for atherosclerosis, however, failed clinical trials due to their unfavorable toxicity profiles, generally caused by high accumulation in nontargeted tissues or in nontargeted cells within the targeted tissues (39). To convert these immunomodulatory small molecules into precision medicines for atherosclerosis, organ-specific and cell-specific delivery is highly desirable.

Our approach allows the creation and immunological screening of a combinatorial nanoparticle library with distinct organ biodistribution and immune cell targeting specificities. By using PET imaging, NIRF, and flow cytometry to generate an extensive database detailing the in vivo performance of the library nanoparticles, we were able to rationally design a strategy that avoids the specific limitations of an immunomodulatory compound. Through this process, we successfully converted a liver-toxic immunomodulatory compound into a precision nanomedicine for atherosclerotic plaque macrophage treatment.

A polymer-core nanoparticle (NP13) in the library has similarly optimal performance to the best-performing NP10 (Fig. S4*A*). Polymer-based nanoparticles have been formulated with chemical compounds (40), peptides (41), and nucleic acids (42). This variety suggests that NP13 may be able to deliver a wide range of therapeutic molecules. In addition, a few nanoparticles (NP3, NP9, and NP10) in the library show high targeting specificity to Ly-$6C^{hi}$ monocytes and DCs, which are attractive targets in certain types of cancer (43), asthma (44), and diabetes (45). It would be interesting to apply the same library screening strategy to develop nanoparticle-based specific drug delivery to these immune cells in relevant diseases.

This nanoparticle library screening strategy in immune cells allowed us to improve the therapeutic index of an immunomodulatory molecule that causes hepatic toxicity and has failed clinical translation. Our precision nanomedicine strategy is radically different from the current clinical therapeutics as well as those in experimental phases. Moreover, the approach's potential to deliver various compounds preferentially to other immune cells would expand its application to numerous immunologically implicated diseases, such as myocardial infarction, diabetes, and cancer.

Materials and Methods

Synthesis of Library Nanoparticles. The compositions of all NP synthesis materials are listed in Table S1. The synthesis procedure for NP1 through NP11 was similar to a previous method (12). Briefly, phospholipids, DiR, and triglyceride were dissolved in a chloroform/methanol solvent, dried to form thin film, and then hydrated with human APOA1 solution. The homogenized solution was sonicated with a tip sonicator, and the aggregates and free lipids were removed by passing through a series of filters. The synthesis procedure for NP12 through NP15 was adapted from a previous microfluidics-based method (14). Briefly, a solution containing 0.79 mL of a PLGA or PLA solution in acetonitrile (100 mg/mL), 1.58 mL of a 3:1 molar ratio of 1,2-dimyristoyl-*sn*-glycero-3-phosphocholine/1-myristoyl-2-hydroxy-*sn*-glycero- phosphocholine (DMPC/MHPC) in ethanol (5 mg/mL), 0.36 mg of DiR, 7.9 mL of ethanol, and 14.5 mL of acetonitrile was prepared. The aforementioned solution was injected in the middle channel of the microfluidic device at a rate of 2 mL/min, and a solution of APOA1 (0.01 mg/mL in PBS) was injected in the outer channels at a rate of 10 mL/min. The product was collected, washed with PBS, and concentrated using tangential filtration [100,000-Da molecular mass cutoff (MMCO)] to remove acetonitrile, ethanol, and lipid-free APOA1. For micelle NP16, 2 mL of chloroform solution containing 211 mg of 1,2-distearoyl-*sn*-glycero-3-phosphoethanolamine-*N*-[amino(polyethylene glycol)-2000] (DSPE-PEG2000) and 0.4 mg of DIR (0.5% mol) was slowly dripped into 10 mL of PBS solution heated at 85 °C under vigorous stirring. After dripping, the solution was kept at 85 °C until all of the chloroform was totally evaporated. The micelle solution was washed and

Downloaded at Palestinian Territory, occupied on November 25, 2021
www.manaraa.com

concentrated in PBS using Millipore centrifugal filter (50,0000 Da MMCO). For liposome NP17, a lipid film was first prepared by evaporating a chloroform solution containing 35.4 mg of 1,2-dipalmitoyl-*sn*-glycero-3-phosphocholine (DPPC), 11.1 mg of DSPE-PEG2000, 10.24 mg of cholesterol, and 0.4 mg of DiR (61.1%, 2%, 33.4%, 0.5% in molar percentage). The residue of chloroform was removed by blowing nitrogen gas. The resulting film was hydrated with 10 mL PBS, vortexed, and subsequently sonicated for 25 min. After centrifugation at 18 × *g* for 10 min to remove aggregates, the liposome solution was washed and concentrated in PBS using Millipore centrifugal filter (100,000 Da MMCO). To oxidize NP1, a PBS solution containing NP1 was stirred at 37 °C in the presence of EDTA, α-tocopherol, and 2,2′-Azo-bis(2-amidinopropane) dihydrochloride for 20 h. The resulting oxidized nanoparticle (NP2) was washed thoroughly with PBS.

Synthesis of GW3965-Loaded Nanoparticles. The synthesis procedure for Rx-HDL was similar to that used for NP10. In addition to phospholipids [POPC and 1-palmitoyl-2-hexadecyl-*sn*-glycero-3-phosphocholine (PHPC), 3:1 by weight] and DiR, GW3965 was added to make up 26% by weight of the total starting materials. For Rx-PLGA-HDL, a solution containing 1 mL of GW3965 in DMSO (50 mg/mL), 2 mL of PLGA (100 mg/mL), 2 mL of lipids (10 mg/mL), 53 mL of acetonitrile, and 22 mL of ethanol was prepared. The organic solution was injected in the middle channel of the microfluidic device at a rate of 2 mL/min, while a solution of APOA1 (0.01 mg/mL in 1× PBS) was injected in the outer channels at a rate of 10 mL/min. The product was collected, washed with PBS, and concentrated to ∼2 mg/mL using tangential and centrifugal filtration (100,000 Da MMCO and 300,000 Da MMCO, respectively). After synthesis, GW9365 was extracted from the final nanoparticles by acetonitrile, and the compound amount was measured by HPLC. The incorporation rate of Rx-HDL was above 90%, and that for Rx-PLGA-HDL was about 50%. The GW3965 injecting dose was adjusted on the basis of the measured GW3965 concentration in the nanoparticle solution.

Animals and Treatment Procedure. All procedures and experiments were approved by the Institutional Animal Care and Use Committee of Icahn School of Medicine at Mount Sinai. About 300 female *Apoe*$^{-/-}$ mice (B6.129P2$^{Apoetm1Unc/J}$) were purchased from Jackson Laboratories and then fed a high-fat diet (Harlan Teklad TD.88137, 42% calories from fat) for 16 wk. These mice developed advanced atherosclerosis in their aortic roots and aortas after 10 wk of high-fat diet and mimicked advanced disease in humans after 16 wk of the diet. Female C57BL/6 mice were fed on regular chow. All nanoparticles were i.v. injected into the lateral tail veins. Care was taken to ensure that each injection was less than 150 μL in volume. For the in vivo characterization study of the 17 nanoparticles, Rx-HDL, and Rx-PLGA-HDL, one i.v. injection was performed. No obvious toxicity or side effects were observed after the injections, except for NP12. After NP12 injection, mice had slow movement, and one out of five died within 24 h after the injection. For short-term toxicity study of Rx-HDL and Rx-PLGA-HDL, four injections in 8 d were given using a GW3965 dose of 10 mg/kg per injection. For the long-term treatment study, the mice received two i.v. injections of Rx-HDL (n = 12) per week for 6 wk at the dose of 10 mg/kg GW3965 per injection or equal volume of PBS (n = 12). A separate cohort of female *Apoe*$^{-/-}$ mice with the same length of high-fat diet received 6 wk of oral GW3965 (n = 6, 10 mg/kg GW3965, two times per week) or PBS (n = 5). No abnormal activities or deaths occurred during the treatment regimen.

Micro-PET/CT Imaging. *Apoe*$^{-/-}$ atherosclerotic mice were injected with either ^{89}Zr-labeled Rx-HDL or Rx-PLGA-HDL at about 200 μCi per mouse (n = 5). At 30 min and 24 h after the injection, the mice were imaged on an Inveon PET/CT scanner (Siemens Healthcare Global) under isoflurane-induced (Baxter Healthcare) anesthesia. Whole-body static PET scans recorded a minimum of 50 million coincident events in ∼15 min. The energy and coincidence timing windows were 350 keV to 700 keV and 6 ns, respectively. The image data were normalized to correct for nonuniform PET response, dead-time count losses, positron branching ratio, and physical decay to the time of injection, but no attenuation, scatter, or partial volume averaging correction was applied. The counting rates in the reconstructed images were converted to activity concentrations (percentage injected dose per gram of tissue) via a system calibration factor derived from imaging a mouse-sized water-equivalent phantom containing ^{89}Zr. Images were analyzed using ASIPro VMTM software (Concorde Microsystems). Activity concentration was quantified by averaging the maximal values of at least 10 regions of interest (ROIs) drawn on consecutive slices of the chosen organs.

Liver mRNA Expression Measurement. Total RNA was obtained from snap-frozen liver tissue and homogenized in TRIzol reagent (Ambion). The homogenate was spun down to pellet tissue, and the aqueous TRIzol supernatant was collected and processed using the Direct-Zol. RNA miniprep kit (Zymo Research Corporation) was used for RNA purification. The RNA was then reverse-transcribed using the Verso cDNA kit (Thermo Scientific) and diluted using RNase/DNase-free water. Quantitative real-time PCR was performed with Taqman Gene Expression Master Mix (Applied Biosystems), and with Taqman primer/probe mixes for *Abca1*, *Abcg1*, or *Srebp1c*. Gene expression was normalized to 18S ribosomal RNA (rRNA) expression.

Aortic Macrophage mRNA Expression Measurement. The quality of RNA extracts from atherosclerotic plaques was measured by Agilent 2100 bioanalyzer (Agilent Technologies). High-quality [RNA integrity number (RIN) > 7] RNA samples were amplified with a WT-Ovation Pico RNA amplification system (NuGen). The cDNA from the amplification reactions were used to run a microfluidics-based mRNA profiling chip (BioMark; Fluidigm), which had high reproducibility. *Hprt1* was used as the housekeeping gene. The following 24 genes were measured: *Abca1*, *Abcg1*, *Srebp1c*, *Nr1h2*, *Hr1h3*, *Ccl2*, *Ccr2*, *Icam1*, *Ifng*, *Il12a*, *Il1a*, *Il1b*, *Il6*, *Nos2*, *Mmp2*, *Mmp9*, *Tnfa*, *Vcam1*, *Ccr7*, *Cd206*, *Foxp3*, *Il10*, *Mrc2*, and *Tgif1*. Twelve biological repeats were included for each gene.

Cellular Lipid Measurement with Flow Cytometry. Single cells were prepared from aortas from either *Apoe*$^{-/-}$ mice or wild-type C57BL/6 mice and then stained with antibody mixtures as described in *SI Materials and Methods*, *Flow Cytometry*. On the basis of a previous procedure (33), the stained cells were washed with PBS two times at room temperature and then incubated with 250 μL PBS containing 0.5 μg/mL BODIPY (D-3922; Molecular Probes) for 15 min. The cells were washed with flow cytometry buffer two times and analyzed in a Becton Dickinson LSRII flow cytometer.

Statistics. Data are presented as mean ± SE of mean (SEM) unless otherwise noted. Two-tailed Student's *t* test was used to calculate statistical significance. GraphPad Prism 5.0 for PC (GraphPad Software Inc.) was used for statistical analysis. $P < 0.05$ was regarded as significant; * denotes P value < 0.05, and ** denotes P value < 0.01 in all figures in the paper.

More description of materials and methods is included in *Supporting Information*.

ACKNOWLEDGMENTS. We thank the flow cytometry core facility, the preclinical imaging center of Translational and Molecular Imaging Institute, and the quantitative qPCR facility of Icahn School of Medicine at Mount Sinai. We thank the small animal imaging core facility, the genomic core facility, the molecular cytology core facility, and the radiochemistry and molecular imaging probe core of Memorial Sloan Kettering Cancer Center. We thank Dr. Kaley Joyes for editing the manuscript. This work was supported by National Institute of Health Grants R01 HL118440, R01HL125703, and R01 CA155432 (to W.J.M.M.), R01 EB009638 (to Z.A.F.), K25 EB016673 (to T.R.), R01HL123433 (to K.J.M.), and P30 CA008748-50 (to Dr. Jason S. Lewis), as well as a Harold S. Geneen Charitable Trust Award (to Z.A.F.), European Framework Program 7 grant (FP7-Health 309820: Nano-Athero) and the Dutch network for Nanotechnology NanoNext NL (A.A. and G.S.), and a Netherlands Organisation for Scientific Research Vidi (to W.J.M.M.).

1. Fridman WH, Pagès F, Sautès-Fridman C, Galon J (2012) The immune contexture in human tumours: Impact on clinical outcome. *Nat Rev Cancer* 12(4):298–306.
2. Lehuen A, Diana J, Zaccone P, Cooke A (2010) Immune cell crosstalk in type 1 diabetes. *Nat Rev Immunol* 10(7):501–513.
3. Moore KJ, Sheedy FJ, Fisher EA (2013) Macrophages in atherosclerosis: A dynamic balance. *Nat Rev Immunol* 13(10):709–721.
4. Swirski FK, Nahrendorf M (2013) Leukocyte behavior in atherosclerosis, myocardial infarction, and heart failure. *Science* 339(6116):161–166.
5. Libby P (2002) Inflammation in atherosclerosis. *Nature* 420(6917):868–874.
6. Heidt T, et al. (2014) Chronic variable stress activates hematopoietic stem cells. *Nat Med* 20(7):754–758.
7. Robbins CS, et al. (2013) Local proliferation dominates lesional macrophage accumulation in atherosclerosis. *Nat Med* 19(9):1166–1172.
8. Galkina E, Ley K (2009) Immune and inflammatory mechanisms of atherosclerosis. *Annu Rev Immunol* 27:165–197.
9. Dutta P, et al. (2012) Myocardial infarction accelerates atherosclerosis. *Nature* 487(7407):325–329.
10. Groot PH, et al. (2005) Synthetic LXR agonists increase LDL in CETP species. *J Lipid Res* 46(10):2182–2191.
11. Kotokorpi P, et al. (2007) Physiological differences between human and rat primary hepatocytes in response to liver X receptor activation by 3-[3-[N-(2-chloro-3-trifluoromethylbenzyl)-(2,2-diphenylethyl)amino]propyloxy]phenylacetic acid hydrochloride (GW3965). *Mol Pharmacol* 72(4):947–955.
12. Tang J, et al. (2015) Inhibiting macrophage proliferation suppresses atherosclerotic plaque inflammation. *Sci Adv* 1(3):e1400223.
13. Duivenvoorden R, et al. (2014) A statin-loaded reconstituted high-density lipoprotein nanoparticle inhibits atherosclerotic plaque inflammation. *Nat Commun* 5:3065.

PNAS PLUS
ENGINEERING
IMMUNOLOGY AND INFLAMMATION
Downloaded at Palestinian Territory, occupied on November 25, 2021
www.manaraa.com

14. Sanchez-Gaytan BL, et al. (2015) HDL-mimetic PLGA nanoparticle to target atherosclerosis plaque macrophages. *Bioconjug Chem* 26(3):443–451.
15. Cormode DP, et al. (2009) HDL as a contrast agent for medical imaging. *Clin Lipidol* 4(4):493–500.
16. Nagano Y, Arai H, Kita T (1991) High density lipoprotein loses its effect to stimulate efflux of cholesterol from foam cells after oxidative modification. *Proc Natl Acad Sci USA* 88(15):6457–6461.
17. Matsumura Y (2008) Poly (amino acid) micelle nanocarriers in preclinical and clinical studies. *Adv Drug Deliv Rev* 60(8):899–914.
18. Torchilin VP (2005) Recent advances with liposomes as pharmaceutical carriers. *Nat Rev Drug Discov* 4(2):145–160.
19. Tall AR, Yvan-Charvet L, Terasaka N, Pagler T, Wang N (2008) HDL, ABC transporters, and cholesterol efflux: Implications for the treatment of atherosclerosis. *Cell Metab* 7(5):365–375.
20. Tall AR, Yvan-Charvet L (2015) Cholesterol, inflammation and innate immunity. *Nat Rev Immunol* 15(2):104–116.
21. Schiener M, et al. (2014) Nanomedicine-based strategies for treatment of atherosclerosis. *Trends Mol Med* 20(5):271–281.
22. Weissleder R, Ntziachristos V (2003) Shedding light onto live molecular targets. *Nat Med* 9(1):123–128.
23. Galkina E, et al. (2007) CXCR6 promotes atherosclerosis by supporting T-cell homing, interferon-gamma production, and macrophage accumulation in the aortic wall. *Circulation* 116(16):1801–1811.
24. Galkina E, et al. (2006) Lymphocyte recruitment into the aortic wall before and during development of atherosclerosis is partially L-selectin dependent. *J Exp Med* 203(5): 1273–1282.
25. Weissleder R, Nahrendorf M, Pittet MJ (2014) Imaging macrophages with nanoparticles. *Nat Mater* 13(2):125–138.
26. Hong C, Tontonoz P (2014) Liver X receptors in lipid metabolism: Opportunities for drug discovery. *Nat Rev Drug Discov* 13(6):433–444.
27. Joseph SB, et al. (2002) Synthetic LXR ligand inhibits the development of atherosclerosis in mice. *Proc Natl Acad Sci USA* 99(11):7604–7609.
28. Naik SU, et al. (2006) Pharmacological activation of liver X receptors promotes reverse cholesterol transport in vivo. *Circulation* 113(1):90–97.
29. Deri MA, Zeglis BM, Francesconi LC, Lewis JS (2013) PET imaging with ^{89}Zr: From radiochemistry to the clinic. *Nucl Med Biol* 40(1):3–14.
30. Zhang SH, Reddick RL, Piedrahita JA, Maeda N (1992) Spontaneous hypercholesterolemia and arterial lesions in mice lacking apolipoprotein E. *Science* 258(5081):468–471.
31. Wu KT, et al. (2016) Nonalcoholic fatty liver disease severity is associated with the ratios of total cholesterol and triglycerides to high-density lipoprotein cholesterol. *J Clin Lipidol* 10(2):420–425.
32. Brunham LR, et al. (2006) Tissue-specific induction of intestinal ABCA1 expression with a liver X receptor agonist raises plasma HDL cholesterol levels. *Circ Res* 99(7): 672–674.
33. Herber DL, et al. (2010) Lipid accumulation and dendritic cell dysfunction in cancer. *Nat Med* 16(8):880–886.
34. Zhao Y, et al. (2016) Augmenting drug-carrier compatibility improves tumour nanotherapy efficacy. *Nat Commun* 7:11221.
35. Mullard A (2015) PCSK9 inhibitors are go. *Nat Rev Drug Discov* 14(9):593.
36. Sabatine MS, et al.; Open-Label Study of Long-Term Evaluation against LDL Cholesterol (OSLER) Investigators (2015) Efficacy and safety of evolocumab in reducing lipids and cardiovascular events. *N Engl J Med* 372(16):1500–1509.
37. Robinson JG, et al.; ODYSSEY LONG TERM Investigators (2015) Efficacy and safety of alirocumab in reducing lipids and cardiovascular events. *N Engl J Med* 372(16): 1489–1499.
38. Chames P, Van Regenmortel M, Weiss E, Baty D (2009) Therapeutic antibodies: Successes, limitations and hopes for the future. *Br J Pharmacol* 157(2):220–233.
39. Cook D, et al. (2014) Lessons learned from the fate of AstraZeneca's drug pipeline: A five-dimensional framework. *Nat Rev Drug Discov* 13(6):419–431.
40. Mieszawska AJ, et al. (2013) Synthesis of polymer-lipid nanoparticles for image-guided delivery of dual modality therapy. *Bioconjug Chem* 24(9):1429–1434.
41. Fredman G, et al. (2015) Targeted nanoparticles containing the proresolving peptide Ac2-26 protect against advanced atherosclerosis in hypercholesterolemic mice. *Sci Transl Med* 7(275):275ra20.
42. Choleris E, et al. (2007) Microparticle-based delivery of oxytocin receptor antisense DNA in the medial amygdala blocks social recognition in female mice. *Proc Natl Acad Sci USA* 104(11):4670–4675.
43. Palucka K, Banchereau J (2012) Cancer immunotherapy via dendritic cells. *Nat Rev Cancer* 12(4):265–277.
44. Hammad H, Lambrecht BN (2008) Dendritic cells and epithelial cells: Linking innate and adaptive immunity in asthma. *Nat Rev Immunol* 8(3):193–204.
45. Mukherjee G, Dilorenzo TP (2010) The immunotherapeutic potential of dendritic cells in type 1 diabetes. *Clin Exp Immunol* 161(2):197–207.
46. Pérez-Medina C, et al. (2015) PET imaging of tumor-associated macrophages with ^{89}Zr-labeled high-density lipoprotein nanoparticles. *J Nucl Med* 56(8):1272–1277.

Downloaded at Palestinian Territory, occupied on November 25, 2021

www.manaraa.com